COLLECTIVE BOUNCE PROBLEMS IN TILTROTORS

Vincenzo Muscarello, Pierangelo Masarati, Giuseppe Quaranta

Department of Aerospace Science and Technology
Politecnico di Milano
Milano, Via La Masa 34, 20156
Italy

Abstract

The basic mechanism of the collective bounce phenomenon on tiltrotors is discussed. This phenomenon may arise if the pilot's biomechanics interact with the airframe elastic modes, in particular with the 1st Symmetric Wing Bending (SWB) mode. A simplified aeroelastic tiltrotor model, able to capture the aircraft heave motion and the low–frequency out-of-plane wing bending dynamics, is proposed. The model, representative of the Bell XV-15, is validated with data reported in literature. The closed-loop pilot-vehicle system shows that the direct effect of a change in collective input results in a nearly immediate change in thrust, which accelerates the tiltrotor exciting the 1st SWB mode and, in turn, the pilot biomechanics generating an unstable feedback path. Robust stability analyses are performed using the Nyquist criterion for SISO systems, considering the feedback loop between the vertical acceleration at the pilot seat and the collective pitch input. Means of prevention, considering both active and passive devices, are investigated and compared with pros and cons.

1 INTRODUCTION

Several pilot-in-the-loop aeroelastic coupling mechanisms have been encountered during the development of tiltrotors, from the early design and testing of the XV-15 technology demonstrator [1] to the V-22 experimental flight tests [2]. On the BA609 (now AW609), the design methodology has benefited from the past experience and pilot-in-the-loop stability analyses have been considered from the early design stage [3], to ensure that the pilot does not degrade the overall stability of the vehicle.

In tiltrotors, as well as in helicopters, the pilot can respond at the structural frequencies creating an unstable feedback path caused by inadvertent or unintentional control inputs, resulting from inertial reactions of the pilot-control devices to the accelerations of the cockpit. These phenomena are called Pilot-Assisted Oscillations (PAOs). The involved vibrations typically occur at frequencies above those of the human operator bandwidth, between 2 and 8 Hz according to Ref. [4]. PAOs phenomena differ from the most widely known Pilot-Induced Oscillations (PIOs), in which the oscillatory behavior of the vehicle results from commands intentionally introduced by the pilot as a result of misinterpreted or contradictory vehicle response cues, e.g. in a frequency range below 1 Hz [5]. As a consequence, while PIO mechanisms are analyzed by means of rigid body vehicle models affecting the flight mechanics modes, PAO phenomena require aeroelastic models in order to represent the higher structural mode frequencies.

Both PIO and PAO phenomena are gathered under the definition of Aircraft-Pilot Couplings (APCs) or Rotorcraft-Pilot Couplings (RPCs) when specifically referred to rotary wing aircraft. PIO and PAO have been widely investigated in relation with fixed-wing aircraft. In recent times, rotary-wing aircraft PIOs received considerable attention. Research on PAO phenomena for rotorcraft is ongoing. In 2007, Walden [6] presented an extensive discussion of aeromechanical instabilities that occurred on several rotorcraft during their development and acceptance by the U.S. Navy, including the CH-46, UH-60, SH-60, CH-53, V-22, and AH-1. A reasonably complete database of PIO and PAO incidents that have occurred to fixed-and rotary-wing aircraft is reported in [5]. Most of those events occurred in the PAO frequency band and involved the involuntary participation of the pilot, often interacting with the Flight Control System (FCS). In many examples, any attempt to reduce the vehicles PAO tendency was conducted on a case-by-case basis, and it was usually addressed by procedural mitigations. Planned structural interventions were either deferred or canceled due to a lack of time or resources.

In this paper a PAO phenomenon peculiar of helicopters is investigated in tiltrotors: the "collective bounce". It's caused by pulsating thrust induced by an oscillation of collective control lever introduced by the pilot. Several studies have been performed on this phenomenon both through numerical analysis [7] and experimental test [8]. The key factor on helicopters has been identified in the reduction of the phase margin of the main rotor coning mode in the collective pitch-heave loop transfer function [9]. Ref. [9] shows that the reduction of stability margins, and the possible development of instability, is rooted in the coupling of the first collective flap (or coning) mode of the main rotor and the

biodynamic mode of the pilots arm holding the collective control inceptor. Helicopters specifically prone to collective bounce phenomena are those with a coning frequency close to the pilot's biomechanical pole at about 2.5–4 Hz; i.e. medium/heavy lift helicopters with long blade spans and low rotor speeds. Recently, a collective bounce phenomenon was experienced by a danish AW101 helicopter during a landing*. Although the crew was not seriously injured the helicopter was heavily damaged.

On classical stiff-in-plane gimballed tiltrotors the coning mode frequency is over the pilot's voluntary/involuntary bandwidth, but the collective bounce phenomenon may still arise if the pilot's biomechanics interact with the airframe elastic modes, in particular with the 1st Symmetric Wing Bending (SWB) mode. In ref. [3] Parham et al. list the frequencies, obtained in NASTRAN, of a detailed AW609 airframe model in airplane and helicopter mode (AP/HE-MODE) configurations. The 1st SWB frequency ranges from 3.35 Hz in APMODE to 3.02 Hz in HEMODE. Similar results are found for the XV-15 [10, 11]. Consequently, the collective bounce may result as a resonance phenomenon between the airframe 1st SWB mode and the pilot's unintentional control input on the collective lever produced by the cockpit vertical accelerations.

Flight test of the V-22 revealed several mechanisms for pilot biomechanical coupling with the airframe dynamics [2], involving a 1.4 Hz lateral oscillation on the ground, a 3.4 lateral oscillation in APMODE and a 4.2 Hz longitudinal oscillation in APMODE. No PAO phenomenon on the vertical axis has been noticed since the V-22 Osprey is not controlled by a collective lever but rather by a Thrust Command Lever (TCL) as conventional fixed wing aircraft. The fore/aft displacement of the TCL decreases the possibility to trigger a PAO phenomenon on the vertical axis. Conversely, on the AW609 civil tiltrotor (as on the XV-15) it was preferred the installation of a Power Lever (PL) that acts as a collective pitch lever in helicopter mode and a thrust control in airplane mode. The vertical displacement of the PL, involuntary introduced by the pilot's limbs, may conceive a vertical load path creating a resonance with the airframe out-of-plane structural dynamics.

2 Modeling pilot-in-the-loop aeroelastic phenomena

Pilot-in-the-loop phenomena can be investigated through the pilot-control device dynamics in feedback loop with the aircraft models. The PVS can be represented in a simple flow block diagram, as shown in Fig. 1. The pilot is generally split in two parts since the control devices are actuated as a consequence of two logically distinct contributions. The first contribution is the result of the intentional, or voluntary, action performed by the pilot to control the vehicle.
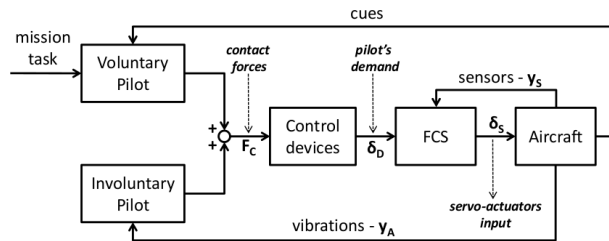
Figure 1: Flow block diagram of the PVS.

Based on the perceived cues, the pilot operates the control devices to perform the desired task. The second contribution originates from vibrations produced by the aircraft and filtered by the pilot's biodynamics. These vibrations come from the interface between the pilot and the cockpit. As a consequence of such excitation, the pilot's arm vibrate while holding the control devices, generating involuntary controls. Voluntary and involuntary pilot's inputs are introduced in the aircraft dynamics by means of the contact forces (F_C) exerted by the pilot on the control devices. The obtained control devices deflections are the pilot's demand (δ_D) that on fly-by-wire aircraft are processed by the Flight Control System (FCS) and subsequently send to the aircraft controls through the servo–actuators input (δ_S). The FCS often plays an important role on pilot-in-the-loop phenomena. It is worth noting that many of the problems discussed in [6] arise because of deficiences in the FCS design where the possibility of indirect pilot activity from other axes contributing to instability in the control law's primary axis has not been considered in an appropriate manner. Thus, it's becoming important to include the FCS on the PVS models to predict pilot-in-the loop phenomena.

The investigation of PAO phenomena requires the introduction of involuntary pilot's models due to their biomechanical properties. Experiments are designed to assess the pilot biodynamic feedthrough (BDFT) in the control inputs due to helicopter vibrations. The term BDFT is referred to a phenomenon where external accelerations are transmitted through the pilot's body causing involuntary limb motions. Several pilot's BDFT have been proposed in the literature using data from cockpit mockup excitation (see, for example, the work by Allen et al. [12], Jex and Magdaleno [13] and Höhne [14]), flight simulator tests (see, for example, the work by Mayo [15] and Masarati et al. [16]), and in–flight measurements (Parham et al. [2]). Numerical models have been proposed by Zanoni et al. [17] for the characterization of the upper limbs of human operators using a multibody approach. The simplest, linear, representation of the pilot's BDFT is reported in the following:

$$(1) \qquad \delta_D = H_{BDFT}(s) \cdot y_A,$$

where the pilot's BDFT is modeled as a transfer matrix (TM) between the accelerations measured at the pilot's seat, i.e. y_A, and the control device deflections (pilot's demand) δ_D obtained as output. Some important remarks must be specified: 1) it is known that humans can adapt

the dynamics of their limbs by adjusting their neuromuscular activity (depending of factors such as task instruction, spatial position and orientation of the human body, see Refs. [18, 19]) and it is likely that these adaptations have a large influence on the BDFT. So, even considering the same pilot the BDFT is not unique; 2) the measured pilot's BDFT also include the control device dynamics. The control forces generated by the pilot must react to the inertia, viscous and elastic restoring forces due to the control device in order to obtain the required deflection. Consequently, although considered separately in the flow block diagram of Fig. 1, the pilot's biomechanics and the control device dynamics are usually part of the same model. An extimation of the pilot's neuromuscular activity can be performed through the measure of the neuromuscular admittance (NMA), which is the dynamic relation between the pilot's control force $\mathbf{F_C}$ and the obtained deflection δ_D. A method to identify the NMA from a detailed multibody model of the left upper limb has been proposed by Zanlucchi et al. in [20] and for both the upper limbs by Zanoni et al. in [21]. Similarly, a novel technique to measure the NMA via experimental tests from motion base simulators has been proposed by Venrooij et al. in [19]. Hence a more complete, but still linear, representation of the pilot's biodynamics should also included the NMA transfer matrix in Eq. 1, namely

$$(2) \qquad \delta_D = \mathbf{H_{BDFT}}(s) \cdot \mathbf{y_A} + \mathbf{H_{NMA}}(s) \cdot \mathbf{F_C}.$$

Some vehicles incorporate digital Fly-By-Wire (FBW) control systems. In tiltrotors this system can be separated into a primary flight control system (PFCS) and an automatic flight control system (AFCS) (see Ref. [2]). The PFCS contains the control laws necessary to maintain mission effectiveness, which include the pilot device gearing functions and rotor governor. The cockpit control devices manipulate the rotor cyclic and collective as well as the aileron, elevator and rudder control surfaces. The PFCS provides the necessary control mixing as a function of airspeed and conversion angle to permit a smooth transition between helicopter and airplane mode flight regimes. The AFCS is designed to enhance flying qualities of the aircraft using feedback path such as pitch and roll rates. Time delays are usually included in the control laws to consider the time taken by electric signals transmitted by the wires and processed by the Flight Control Computer (FCC) to reach the servo-actuator inputs. Again the simplest, linear, representation of the FCS control laws can be described by two transfer matrices, namely

$$(3) \qquad \delta_S = \mathbf{H_{PFCS}}(s) \cdot \delta_D + \mathbf{H_{AFCS}}(s) \cdot \mathbf{y_S},$$

representing the control laws related to the PFCS as a function of the pilot's demand (δ_D) and the control laws related to the AFCS as a function of the aircraft sensors ($\mathbf{y_S}$). The output of the FCS model is due to the servo-actuator input, i.e. δ_S.

The aircraft model for PAO stability analyses can be also represented as a linear system about a reference (trim) condition, described by the transfer matrix between the servo-actuator input δ_S and the output vector $\mathbf{y} = \{\mathbf{y_S}, \mathbf{y_A}, \dots\}$ containing the measures to close the feedback loop with the pilot and the FCS, namely:

$$(4) \qquad \mathbf{y} = \mathbf{H_{A/C}}(s, \mathbf{p}) \cdot \delta_S,$$

where the vector $\mathbf{p}$ contains the trim condition.

In the following, the transfer functions of Eqs. 1, 2, 3 and 4 will be defined for the Bell XV-15 tiltrotor, at the hover, sea-level standard (SLS) flight condition. The collective bounce phenomenon will be investigated considering only the main vertical dynamics. Moreover, the PVS will be reduced to a SISO system considering only the direct path between the power lever deflection as pilot's demand, $\delta_D = \delta_{PL}$, and the vertical acceleration measured at the pilot's seat, namely $\mathbf{y_A} = a_z^{seat}$.

2.1 Aeroelastic tiltrotor model

To analyze the collective bounce phenomenon on tiltrotors a simple, analytical, model representing the aircraft heave motion and the low–frequency out-of-plane wing bending dynamics has been proposed. Due to the tiltrotor symmetry only half of the structure has been analyzed, as sketched in Fig. 2. The semi-span wing has been modeled as an elastic beam of lenght l and constant out-of-plane bending stiffness EI_{xx}, constrained to the plane of simmetry through a slider. The model is based on the XV-15 geometry, weights and wing structural characteristics reported in Ref. [11]. Two concentrated masses, located on the root (M_1) and on the tip of the wing (M_2), represent the fuselage–empennages and the nacelle–rotor bodies. The mass per unit-of-length of the semi-span wing has been lumped on its edges, so also included in M_1 and M_2, in order to obtain a simple analytical solution of the elastic problem. This approximation is considered acceptable to capture the low-frequency wing bending dynamics, since the wing mass is lower to the fuselage–empennages, nacelle and rotor masses placed on the wing edges. The percentage of lumped wing mass has been selected in order to improve the correlation with the modal mass and the mode shape of the 1st SWB mode of the XV-15 tiltrotor reported in Ref. [11]. Finally, a lumped inertia about the global x axis has been placed on the tip of the wing, i.e. $J_{xx}(\beta_n)$, including the contribution of the nacelle–rotor bodies as a function of the nacelle angle β_n ranging from 0 (APMODE) to 90 (HEMODE) degrees.

The kinematic of the wing is described as a function of the vertical displacement at the wing root $z(t)$ and of the vertical elastic deflection of the wing $w(y,t)$. The total vertical displacement is due to the sum of the two contributions. The elastic wing is modeled with the Euler-Bernoulli beam theory and the tiltrotor structural model can be ob-
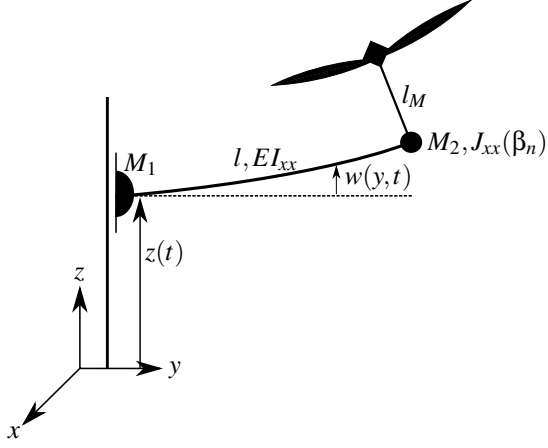
Figure 2: Sketch of the simplified tiltrotor model.

tained by the Principle of Virtual Work (PVW), namely:

$$(5) \quad \delta W = -\delta z M_1 \ddot{z} - (\delta z + \delta w_l) M_2 (\ddot{z} + \ddot{w}_l) - \delta w_l' J_{xx} \ddot{w}_l'$$
$$- \int_0^l \delta w'' EI_{xx} w'' dy = 0,$$

where it was introduced the term $w_l = w(l,t)$, i.e. the elastic deflection evaluated at the wing tip, to condense the equation of the PVW. Integrating by parts the elastic term of Eq. 5, applying the boundary conditions at the wing root, i.e. $w(0,t) = w'(0,t) = 0$, and considering arbitrary virtual displacements the following set of differential equations is obtained:

$$(6a) \qquad EI_{xx} \frac{d^4 w}{dy^4} = 0,$$

$$(6b) \qquad (M_1 + M_2) \ddot{z} + M_2 \ddot{w}_l = 0,$$

$$(6c) \qquad M_2 (\ddot{z} + \ddot{w}_l) - EI_{xx} w_l''' = 0,$$

$$(6d) \qquad J_{xx} \ddot{w}_l' + EI_{xx} w_l'' = 0.$$

The integration of Eq. 6a returns a cubic solution for the elastic deflection of the wing, namely:

$$(7) \qquad w(y,t) = w_1(t) \frac{y^3}{6} + w_2(t) \frac{y^2}{2},$$

depending of the two time functions $w_1(t)$ and $w_2(t)$. Substituting the obtained solution on Eqs. 6b, 6c and 6d and projecting the equations in a symmetric subspace, the following second order model is obtained:

$$(8)$$
$$\begin{bmatrix} M_1 + M_2 & M_2 \frac{l^3}{6} & M_2 \frac{l^2}{2} \\ M_2 \frac{l^3}{6} & M_2 \frac{l^6}{36} + J_{xx} \frac{l^4}{4} & M_2 \frac{l^5}{12} + J_{xx} \frac{l^3}{2} \\ M_2 \frac{l^2}{2} & M_2 \frac{l^5}{12} + J_{xx} \frac{l^3}{2} & M_2 \frac{l^4}{4} + J_{xx} l^2 \end{bmatrix} \begin{Bmatrix} \ddot{z} \\ \ddot{w}_1 \\ \ddot{w}_2 \end{Bmatrix}$$
$$+ EI_{xx} \begin{bmatrix} 0 & 0 & 0 \\ 0 & \frac{l^3}{3} & \frac{l^2}{2} \\ 0 & \frac{l^2}{2} & l \end{bmatrix} \begin{Bmatrix} z \\ w_1 \\ w_2 \end{Bmatrix} = \mathbf{0},$$

describing the tiltrotor vertical dynamics in vacuum. The model of Eq. 8 is used to evaluate frequencies and mode shapes in vacuum for different tiltrotor configurations, updating the nacelle–rotor inertia J_{xx} as a function of the nacelle angle β_n.

The aerodynamic database is provided only in hover condition, with $\beta_n = 90$ deg., including the rotor stability and control derivatives due to the rotor thrust force and the axial inflow dynamics described by Pitt-Peters in [22]. A simple perturbation model of the download acting on the wing is also included. The steady aerodynamic model must be able to capture the heave time constant and the 1st SWB aerodynamic damping. Rotor dynamics are not taken into account since their contribution is considered faster then the analyzed airframe dynamics, thus negligible for modeling the collective bounce phenomenon.

A steady, linearized, contribution of the thrust force produced by the rotor for the tiltrotor vertical dynamics includes the stability derivatives with respect to the vertical velocity measured at the rotor hub $\dot{z}_H$ and the axial (uniform) inflow λ_u, plus the control derivative due to the collective pitch ϑ_0:

$$(9) \qquad \Delta T = -T_{/\dot{z}_H} \dot{z}_H - T_{/\lambda_u} \lambda_u + T_{/\vartheta_0} \vartheta_0,$$

where the vertical velocity measured to the rotor hub is considered equal to the vertical velocity of the wing tip, i.e. $\dot{z}_H = \dot{z} + \dot{w}_l$. The virtual work due to the thrust perturbation, i.e. $\delta W = (\delta z + \delta w_l) \Delta T$, returns a damping matrix

$$(10) \qquad \mathbf{C}_1 = T_{/\dot{z}_H} \begin{bmatrix} 1 & \frac{l^3}{6} & \frac{l^2}{2} \\ \frac{l^3}{6} & \frac{l^6}{36} & \frac{l^5}{12} \\ \frac{l^2}{2} & \frac{l^5}{12} & \frac{l^4}{4} \end{bmatrix},$$

and two input vectors

$$(11) \qquad \mathbf{f}_1 = -T_{/\lambda_u} \begin{bmatrix} 1 \\ \frac{l^3}{6} \\ \frac{l^2}{2} \end{bmatrix} \lambda_u + T_{/\vartheta_0} \begin{bmatrix} 1 \\ \frac{l^3}{6} \\ \frac{l^2}{2} \end{bmatrix} \vartheta_0,$$

to be added at the second order model of Eq. 8. The thrust coefficients reported in Eq. 9 are obtained in this work through the blade element theory, as shown in the next section.

The download perturbation is modeled as a vertical drag force distributed on the external sections of the tiltrotor wing as shown in Fig. 3. The dynamic pressure is due to the the rotor wake induced velocity impacting downstream on the wing added to the wing vertical velocity, i.e. $v_w + (\dot{z} + \dot{w})$. During an hover flight condition, the rotor wake induced velocity impacting on the wing v_w is related to the rotor disk induced velocity v through the conservation of mass, namely $Av = A_w v_w$ (incompressible and inviscid flow), where $A = \pi R^2$ is the rotor disk area and $A_w = \pi R_w^2$ is the rotor wake area at the wing level. The induced velocity v_w can be written as a function of the in-
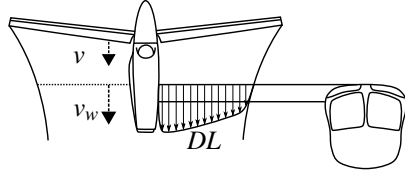
(a) Frontal view.
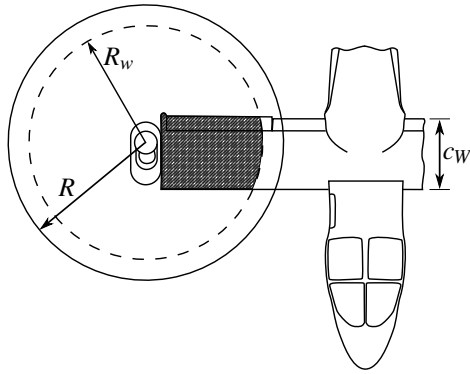
(b) Top view.

Figure 3: Tiltrotor wing subjected to download.

duced velocity v and of the ratio of the two areas as:

$$(12) \qquad v_w = v \left(\frac{A}{A_w} \right) = v \left(\frac{R}{R_w} \right)^2,$$

where it can be defined the contraction factor $k = A/A_w = R^2/R_w^2$. The download in hover condition can be evaluated

through the strip theory integrating the download force per unit of length along the external wing span:

$$(13) \qquad DL_H = \int_{l-R_w}^{l} \frac{1}{2} \rho v_w^2 c_W(y) C_{DL} dy,$$

where $c_W(y)$ is the tiltrotor wing chord, here considered constant. The aerodynamic download coefficient, C_{DL}, is roughly extimated as the drag coefficient of 2D flat plate perpendicular to flow ($C_{DL} = 2$, see Chapter 1 of Ref. [23]), since the rotor wake is approximately orthogonal to the wing surface, obtaining:

$$DL_H \approx \frac{1}{2} \rho v_w^2 c_W R_w C_{DL},$$
$$\approx \frac{1}{2} \rho k^2 v c_W \frac{R}{\sqrt{k}} C_{DL},$$
$$(14) \qquad \approx \frac{1}{2} \rho k^{3/2} v c_W R C_{DL}.$$

In hover condition the download ranges from 10% to 15% of the overall tiltrotor weight, hence from the knlowledge of DL_H is possible to reverse Eq. 14 to obtain the contraction factor k. When considering the total velocity the download becomes:

$$(15) \qquad DL = \int_{l-R_w}^{l} \frac{1}{2} \rho \left(v_w + \dot{z} + \dot{w} \right)^2 c_W(y) C_{DL} dy,$$

and the linearized contribution about the hover trim condition on the PVW returns:

$$(16)$$
$$\delta W = - \int_{l-R_w}^{l} (\delta z + \delta w) \rho k v \left(k \Omega R \lambda_u + \dot{z} + \dot{w} \right) c_W(y) C_{DL} dy,$$

where the rotor induced velocity perturbation has been introduced as a function of the dimensionless inflow ratio $\lambda_u = \Delta v / (\Omega R)$. Once defined the download coefficient per unit of length, $DL_{/V} = \rho k v c_W C_{DL}$, containing all the constant contributions of Eq. 16, the PVW returns a further damping matrix

$$(17) \qquad \mathbf{C}_2 = DL_{/V} \begin{bmatrix} R_w & \frac{1}{24} \left(l^4 - (l-R_w)^4 \right) & \frac{1}{6} \left(l^3 - (l-R_w)^3 \right) \\ \frac{1}{24} \left(l^4 - (l-R_w)^4 \right) & \frac{1}{252} \left(l^7 - (l-R_w)^7 \right) & \frac{1}{20} \left(l^5 - (l-R_w)^5 \right) \\ \frac{1}{6} \left(l^3 - (l-R_w)^3 \right) & \frac{1}{20} \left(l^5 - (l-R_w)^5 \right) & \frac{1}{72} \left(l^6 - (l-R_w)^6 \right) \end{bmatrix},$$

and an input vector as a function of the dimensionless inflow:

$$(18) \qquad \mathbf{f}_2 = -DL_{/V} k\Omega R \begin{bmatrix} R_w \\ \frac{1}{24}\left(l^4 - (l - R_w)^4\right) \\ \frac{1}{6}\left(l^3 - (l - R_w)^3\right) \end{bmatrix} \lambda_u.$$

The steady aerodynamic contributions due to the thrust and download perturbation are added to the mass and stiffness matrices of Eq. 8. Once defined the state vector $\mathbf{u} = \{z, w_1, w_2\}^T$ and its time derivatives, the second order model takes the form:

$$(19) \qquad \mathbf{M\ddot{u}} + (\mathbf{C_1} + \mathbf{C_2})\,\dot{\mathbf{u}} + \mathbf{Ku} = \mathbf{f_1} + \mathbf{f_2}.$$

The first order inflow model described by Pitt–Peters [22] is added to Eq. 19 to consider the rotor unsteady aerodynamics due to the rotor wake–induced volocity. To capture the tiltrotor vertical dynamics only the axial (uniform) contribution λ_u of the three inflow states is included, described by the scalar equation reported in the following:

$$(20) \qquad L_u M_u \dot{\lambda}_u + \lambda_u = L_u \hat{C}_T,$$

with the apparent mass equal to $M_u = \frac{128}{75\pi}$ and $L_u = \frac{1}{4}\frac{\Omega R}{v}$ for the hover configuration. The thrust coefficient also includes the effects of the rotor hub motion, namely:

$$(21) \qquad \hat{C}_T = \Delta C_T - C_{T_H}\frac{\dot{z}_H}{v},$$

where the first term includes the dimensionless thrust perturbation of Eq. 9, i.e. $\Delta C_T = \frac{\Delta T}{\rho(\Omega R)^2 A}$, and C_{T_H} is referred to the thrust coefficient in hover condition.

The proposed aeroelastic model is characterized only by the collective pitch as input. Servo–actuators are not included at this preliminary stage since the servo–valve dynamics are characterized by higher bandwidth when compared to the collective bounce phenomenon. The aircraft input can be directly considered as $\delta_\mathbf{S} = \vartheta_0$. Similarly, only the vertical acceleration at the pilot's seat, formally equal to the acceleration measured at the wing root $\mathbf{y_A} = a_z^{seat} = \ddot{z}$, is considered as output, returning a SISO model. The aircraft transfer matrix of Eq. 4 becomes a simple transfer function:

$$(22) \qquad \ddot{z} = H_{\ddot{z}\vartheta_0}\left(s, \mathbf{p_H}\right)\vartheta_0,$$

with the trim parameter vector evaluated at the hover condition $\mathbf{p_H}$.

The FCS is extremely simplified. In HEMODE, the PFCS includes only the gear ratio G_0 between the power lever displacement and the collective pitch rotation. Time delays can be introduced when considering FBW architectures, as for the V-22 or for the AW609. On the XV-15 tiltrotor, pilot's controls were instantly trasmitted to the servo–actuators through mechanical linkages [24] without passing to the FCC processing (although they occupied the whole passenger cabin). Control laws on the vertical dynamics are usually not necessary, since they are asymptotically stable and easily controlled by the pilot. Hence, the proposed model is not characterized by the AFCS simplifying Eq. 3 through a scalar gain, i.e. $\vartheta_0 = G_0 \delta_{PL}$.

2.2 Validation of the numerical model

The proposed aeroelastic tiltrotor model for collective bounce analysis is based on the Bell XV-15, since the required data are available from the open literature. The structural characteristics are taken by the XV-15 finite element stick model of Ref. [11] and here reported in Table 1.

The two lumped masses on the wing edges and the inertia on the wing tip have been evaluated considering the tiltrotor symmetry about the xz plane, namely:

$$(23a) \qquad M_1 = \frac{1}{2}\left(M_F + k_w M_W\right),$$

$$(23b) \qquad M_2 = \frac{1}{2}\left(M_R + M_N + (1 - k_w)M_W\right),$$

$$J_{xx}(\beta_n) = J_{N_{\hat{x}\hat{x}}}cos^2\beta_n + J_{N_{\hat{z}\hat{z}}}sin^2\beta_n$$
$$(23c) \qquad - J_{N_{\hat{x}\hat{z}}}sin2\beta_n + \frac{1}{2}M_R\left(l_M sin\beta_n\right)^2,$$

where k_w represents the percentage of wing mass lumped on the wing edges ranging from 0 to 1, and initially set to $k_w = 0.5$. The inertia on the wing tip includes the nacelle contribution, reported in the global reference frame[†], and the inertia due to the rotor mass transport contribution. The numerical values of k_w and EI_{xx} have been modified in order to reach the frequency and modal mass of the 1st SWB mode of the detailed XV-15 Finite Element Model (FEM) reported in Table 3 of Ref. [11], considering the APMODE configuration, i.e. $\beta_n = 0$ deg. Results are reported in Table 2. The initial data return a smaller frequency and an higher modal mass when compared with the detailed FEM model results. To decrease the modal mass an higher percentage of wing mass has been lumped on the wing root ($k_w = 0.5 \rightarrow 0.8$) while to increase the 1st SWB frequency the wing beam stiffness has been augmented from $EI_{xx} = 3.70E{+}09$ lb-in^2 to $EI_{xx} = 4.40E{+}09$ lb-in^2. Mode shapes have been rescaled in order to consider the maximum displacement equal to the unity. The updated configuration

---

[†]The local nacelle reference frame is aligned with the global reference frame in APMODE. It can rotate with the nacelle angle β_n about the wing-span axis.

Table 1: XV-15 Structural model characteristics.

| XV-15 Characteristic	Symbol	Value	Units
Fuselage mass[a]	M_F	6182.00	lb
Wing mass[b]	M_W	2534.00	lb
Left and right rotor masses	M_R	1118.00	lb
Left and right nacelle masses	M_N	3166.00	lb
Gross weight	M_T	13000.00	lb
Nacelle inertia about $\hat{x}$ axis	$J_{N_{\hat{x}\hat{x}}}$	100.00	slug-ft^2
Nacelle inertia about $\hat{z}$ axis	$J_{N_{\hat{z}\hat{z}}}$	450.00	slug-ft^2
Nacelle product of inertia	$J_{N_{\hat{x}\hat{z}}}$	0.00	slug-ft^2
Rotor mast length	l_M	4.67	ft
Wing semi–span length	l	16.08	ft
Wing beam stiffness	EI_{xx}	3.70E+09	lb-in^2

[a] Includes empennages, equipment, crew and payload.
[b] Includes fuel, cross shafting, etc.

Table 2: 1st SWB – Eigenanalysis results.

	FEM Model[a]	Proposed Model Initial Data	Proposed Model Updated Data
Percentage of wing mass lumped k_w, n.d.	-	0.5	0.8
Wing beam stiffness EI_{xx}, lb-in^2	-	3.70E+09	4.40E+09
Frequency, Hz	3.4	3.1	3.4
Modal mass, slug	241.6	306.4	241.6
Displacement at the wing tip, ft/ft	1.0000	1.0000	1.0000
Rotation at the wing tip, rad/ft	0.1463	0.1637	0.1486

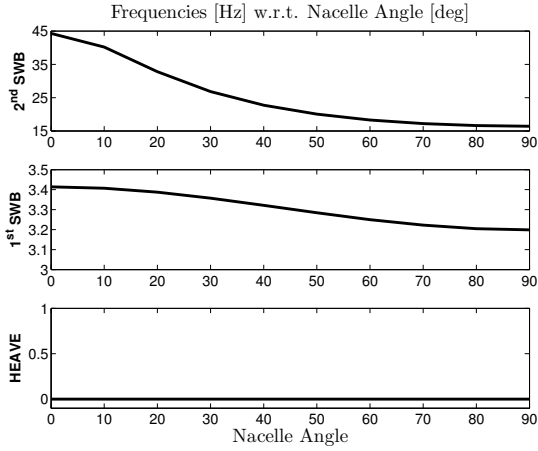[a] See Table 3 of Ref. [11].
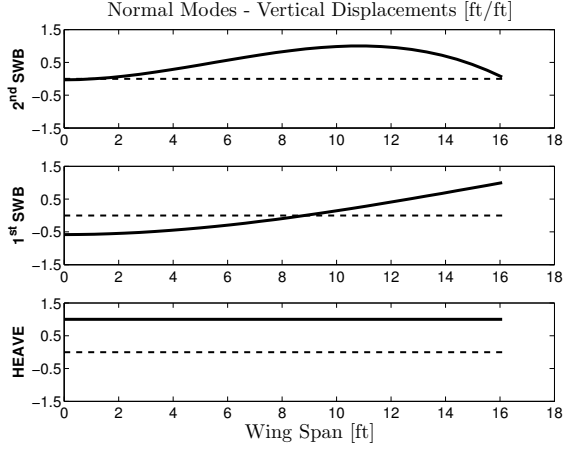
(a) Normal modes in APMODE.

(b) Frequencies w.r.t. Nacelle Angle, β_n

Figure 4: Eigenanalysis in vacuum.

also shows a good agreement in terms of rotation at the wing tip. Mode shapes in APMODE and frequencies as a function of the nacelle angle are shown in Fig. 4. The model is able to capture the rigid heave motion, the first and second symmetric wing bending modes of the tiltrotor. It must be remembered that the proposed model was developed in order to tune only the 1st SWB. The higher frequency of the 2nd SWB is the result of the concentrated inertia on the wing tip, necessary to update the normal modes as a function of the nacelle angle, although it can

not be considered representative of the real XV-15 due to the model simplicity. Fig. 4(b) also shows how the SWB frequencies decrease with the nacelle angle. This is the direct consequence of increasing the wing tip inertia when passing from APMODE to HEMODE. In particular, the 1st SWB ranges from 3.4 Hz in APMODE to 3.2 Hz in HEMODE.

The thrust stability and control derivatives in hover, SLS condition, have been roughly estimated with the blade element theory considering blade constant contributions (see for example chapter 2 of [25]), namely:

$$(24a) \qquad T_{/\dot{z}_H} = \frac{B_T^2}{4R^2} \gamma N_b \Omega I_b,$$

$$(24b) \qquad T_{/\lambda_u} = \frac{B_T^2}{4R} \gamma N_b \Omega^2 I_b,$$

$$(24c) \qquad T_{/\vartheta_0} = \frac{B_T^3}{6R} \gamma N_b \Omega^2 I_b.$$

Due to the tiltrotor symmetry, the thrust coefficient has been calculated considering half of the gross weight reported in Table 1,

$$(25) \qquad C_{T_H} = \frac{M_T g/2}{\rho \left(\Omega R \right)^2 A^2},$$

and the induced velocity with the actuator disk theory, namely

$$(26) \qquad \frac{v}{\Omega R} = \kappa_h \sqrt{\frac{C_{T_H}}{2}},$$

where an empirical inflow correction factor of $\kappa_h = 1.2$ has been taken into account. The XV-15 aerodynamic characteristics in Eqs. 24, 25 and 26 have been extracted by the work of S.W. Ferguson [26] (see Appendix B) and here reported in Table 3.

Including the aerodynamic data, the eigenanalysis of the aeroelastic (AE) system returns a stable vehicle characterized by a real pole representing the rigid heave dynamics and two complex and conjugates roots for the first and second symmetric wing bending modes. The time constant of the rigid heave dynamics has been compared with the results obtained by S. W. Ferguson with the Generic Tiltrotor simulation (GTRs) code in [27] and with the results identified by M. B. Tischler during an experimental test campaign of the XV-15 with CIFER [28]. The eigenvalues

Table 3: XV-15 Aerodynamic model characteristics.

XV-15 Characteristic	Symbol	Value	Units
Number of blades per rotor	N_b	3	n.d.
Rotor radius	R	12.50	ft
Flapping inertia per blade	I_b	102.50	slug-ft^2
Rotor speed (HEMODE)	Ω	589.00	rpm
Lock number	γ	3.83	n.d.
Tip loss factor	B_T	0.97	n.d.
Empirical inflow correction factor in hover	κ_h	1.20	n.d.
Wing chord	c_W	5.25	ft

Table 4: Aeroelastic roots

	GTRs	CIFER	AE Model W/out download	AE Model With download
Heave-mode time constant, sec	4.99	9.52	5.01	4.32
1st SWB Frequency, Hz	-	-	3.18	3.18
1st SWB Damping^a, %	-	-	3.86	3.90

^{a} Includes a 3% of structural damping [11].

are listed in Table 4. Frequency and damping of the 1st SWB mode are also reported for the AE model, including the structural damping of 3% as described by Acree et al. in [11]. Results obtained with the GTRs and CIFER represent only the rigid, low frequency, behavior of the XV-15. The comparison of the heave-mode time constant shows a good correlation with the GTRs data but a poor correlation with the flight-extracted results identified by CIFER. Both the GTRs code and the AE model underestimate the heave-mode time constant. Tiltrotor class vehicles, in contrast to single-rotor helicopters, are characterized by very long time-constants due to the higher disk loading [28] and probably the representation of the aerodynamic loads on the GTRs code and on the AE model is not sufficiently accurate to correctly capture the heave dynamics.

The aerodynamic forces slightly increase the damping of the 1st SWB. A small contribution of less than 1% is added to the prescribed structural damping (3%). The aerodynamic damping in hover is mainly produced by the rotors and the wing does not generate any aerodynamic contribution. It is the small damping of the 1st SWB mode in hover making more prone the vehicle to the instability with the close pilot's biomechanical pole. Including the wing download, the 1st SWB damping weakly increases (+ 0.04%) while the heave-mode time constant is reduced from 5.01 to 4.32 sec.

The transfer function (TF) of the vertical acceleration response $\ddot{z}$ to the power-lever δ_{PL} is reported in Fig. 5(a). The bode plot shows the TF of the proposed AE model with analogs results obtained with the GTRs and CIFER. The comparison is made in a frequency range up to 1 Hz since the GTRs and CIFER do not represent the higher aeroelastic frequency content. Again, there is a good correlation between the results of the AE model and the GTRs code, proving that both models are able to develop the same control forces. Conversely, the magnitude of the TF identified by CIFER results lower, demonstrating that the numerical

models overestimate the control forces produced by the rotors. One of the main reason is probably the lack of the rotor blade pitch dynamics, including the effect of the control chain compliance, which could justify the higher value of the control derivative T_{ϑ_0} on the numerical models. In this case, the static residualization of the blade pitch dynamics should improve the correlation with the flight test data, although an higher value of the control derivative T_{ϑ_0} is conservative for the analysis of the collective bounce phenomenon, especially during the vehicle design. The effect of the higher control forces predicted by the numerical model is also shown in Fig. 5(b), where the time response to the power-lever input is obtained directly from flight test data and compared with the results obtained by the model identified by CIFER and with the proposed AE model. The AE model is able to capture the general trend recorded during the flight test even though it shows higher values of the vertical acceleration at the same power-lever input. Finally, it should be noted that the flight test data also show an higher frequency contribution probably related to the 1st SWB between 21–25 seconds.

## 2.3 Pilot-control device biomechanical models

In [15], Mayo identified the BDFT of a human body to describe the involuntary action of helicopter pilots on the collective control inceptors when subjected to vertical vibration of the cockpit. In particular, Mayo identified the TFs between the absolute vertical acceleration of the pilot hand, $\ddot{z}_{h.abs}$, as a function of the vertical acceleration of the vehicle, $\ddot{z}$. As discussed in [9], these TFs need to be written as the relative acceleration of the hand, $\ddot{z}_{hand}$, with respect to the vehicle acceleration, namely

$$(27) \qquad \ddot{z}_{hand} = \ddot{z}_{h.abs} - \ddot{z} = -s \frac{s + 1/\tau_p}{s^2 + 2\xi_p \omega_p s + \omega_p^2} \ddot{z}.$$
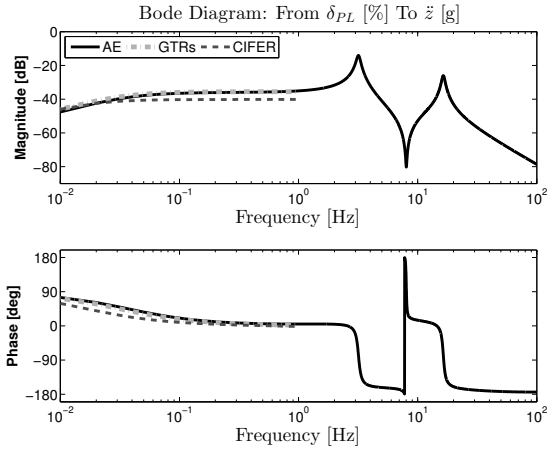
(a) Transfer Function (see Fig. 4.27, pag. 85, of Ref. [28]).
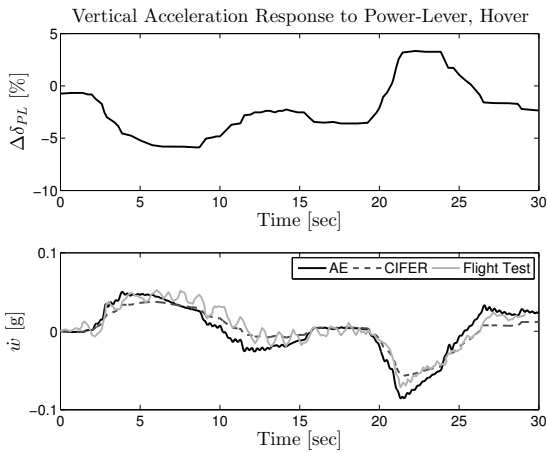
(b) Time Response (see Fig. 4.34, pag. 97, of Ref. [28]).

Figure 5: Vertical acceleration response to power-lever input.

Two set of pilots have been investigated by Mayo, called ectomorphic (small and lean build) and mesomorphic (large bone structure and muscle build). The structural properties of the Mayo's ectomorphic and mesomorphic TFs are reported in Table 5. It should be remembered that the TF of Eq. 27 must be integrated twice to yield the relative displacement of the hand, $z_{hand} = \ddot{z}_{hand}/s^2$. However, the double integration gives an integrator-like low-frequency asymptotic behavior, $1/s$, that is not physical (a pilot would always be able to compensate the error corresponding to a slow enough input) and overlaps with the pilot's voluntary behavior [9]. The low-frequency asymptotic behavior can be corrected by adding a second-order high-pass filter with cutoff frequency ω_h slightly above the crossover frequency ω_c of the voluntary pilot's model. Since ω_c is less than 0.5 Hz, while the pilot's biomechanical poles are at about 3.5 Hz, the bands of interest of the pilot's voluntary and involuntary models should be adequately separated. The combination of the double integra-

Table 5: Structural properties of Mayo's TFs.

Ectomorphic Pilot	Symbol	Value	Units
Frequency	ω_p	3.380	Hz
Damping ratio	ξ_p	32.000	%
Time constant	τ_p	0.117	sec
Mesomorphic Pilot	Symbol	Value	Units
Frequency	ω_p	3.750	Hz
Damping ratio	ξ_p	28.000	%
Time constant	τ_p	0.107	sec

tion and high-pass filtering yields

$$(28) \qquad H_{BDFT}(s) = -\frac{s}{(s+\omega_h)^2} \frac{s+1/\tau_p}{s^2 + 2\xi_p\omega_p s + \omega_p^2},$$

where a numerical value of ω_h = 3.10 rad/s has been used in Eq. 28. The maximum vertical displacement of the XV-15 power-lever inceptor, z_{hand}^{MAX} = 10.0 inches (see Ref. [26]), has been used to obtain a dimensionless output of Eq. 28. The poles associated with the pilot's BDFT are well damped (about 30%). The frequency is about 3.5 Hz, compared with the "three cycles per second" mentioned in the collective bounce accidents[‡].

Pilot's BDFT have been identified also from flight simulator tests by Masarati et al. in [16], where TFs have been parameterized for 3 different collective lever reference positions (10%, 50% and 90%) and obtained for two pilots, showing two resonant peaks respectively in the 2–4 and in the 5–7 Hz ranges. The identified TFs are structurally different from that of Eq. 28 (four poles and two zeros) but with identical high frequency asymptotic behavior and with the lower biodynamic pole similar to those that appear in Mayo's TFs; the interested reader is referred to that document for further details.

A pilot-control device model in the form of Eq. 2 can be obtained through a rational representation of both the BDFT and NMA transfer functions, consisting of a second-order low-pass filter in the band of interest (1-10 [Hz]) as suggested by Zanlucchi et al. in [20], namely:

$$(29) \qquad H_{(\cdot)}(s) = \frac{b_{(\cdot)}}{s^2 + a_1 s + a_2},$$

with $(\cdot)$ corresponding to BDFT and NMA. Eq. 29 can be used to describe the basic pilot biomechanical behavior and also to analyze the effects of modifications to the dynamics of the control inceptor on the overall dynamics of the vehicle. In this work, the TFs coefficients have been tuned considering the Mayo's models as starting point. In particular:

- the denominator coefficients a_1, a_2 have been defined in order to obtain the same damping and characteristic frequency of the Mayo's biomechanical poles, i.e. $a_2 = \omega_p^2$ and $a_1 = 2\xi_p\omega_p$;

[‡]NTSB reports SEA08LA043 and ANC08LA083, see the webpage: http://www.ntsb.gov
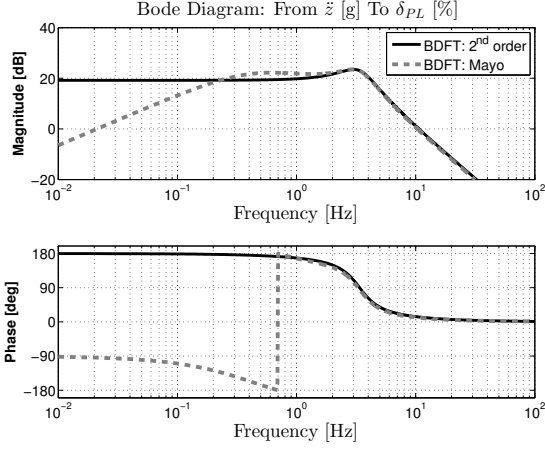
(a) Biodynamic Feedthrough (BDFT).
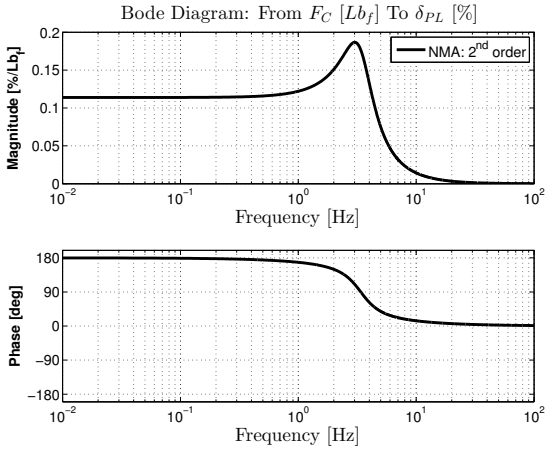
(b) Neuromuscular Admittance (NMA).

Figure 6: Pilot-control device second-order numerical model of Mayo's ectomorphic TF.

- the BDFT numerator b_{BDFT} has been defined in order to perfectly match the Mayo's pilot biomechanical magnitude at the characteristic frequency, i.e. $b_{BDFT} \rightarrow \|H_{BDFT}(j\omega_p)\|$, where ω_p is the frequency of the biodynamic pole (see Fig. 6(a));

- the NMA numerator b_{NMA} has been calculated in order to obtain a force gradient, considering a static reference condition, of about $9 \, Lb_f/\%$.

The identified coefficients of the second-order pilot-control device BDFT and NMA TFs are reported in Table 6 considering ectomorphic and mesomorphic pilot's characteristics. It should be noted that also the proposed second-order pilot-control device model overlaps with the pilot's voluntary behavior. The introduction of an high-pass filter, with a cut-off frequency above the crossover frequency, can be used to solve this problem.

The knowledge of the NMA allows to modify the control device dynamics. For example, it is possible to include an hydraulic damper in the power-lever to decrease the collective bounce proneness. Considering a linear damper, the

Table 6: Structural properties of second-order pilot-control device model.

Ectomorphic Pilot	Symbol	Value	Units
Denominator	a_2	452.30	(rad/sec)^2
Denominator	a_1	13.70	rad/sec
Numerator BDFT	b_{BDFT}	-1.07	rad^2
Numerator NMA	b_{NMA}	-5.15	rad^2/slinch
Mesomorphic Pilot	Symbol	Value	Units
Denominator	a_2	555.40	(rad/sec)^2
Denominator	a_1	13.31	rad/sec
Numerator BDFT	b_{BDFT}	-1.07	rad^2
Numerator NMA	b_{NMA}	-6.90	rad^2/slinch

pilot's force acting on the control device will be characterized by two contributions, namely:

$$(30) \qquad F_C = C\dot{\delta}_{PL} + \hat{F}_C,$$

where the first term is the viscous force produced by the damper and the second contribution an additional force acting on the device. Applying Eq. 30 in the second-order pilot-control device model, the following transfer functions are obtained:

$$(31) \quad \delta_{PL} = \frac{b_{BDFT}}{s^2 + a_1 s + a_2}\ddot{z} + \frac{b_{NMA}}{s^2 + a_1 s + a_2}\left(Cs\delta_{PL} + \hat{F}_C\right),$$

which yields an updated pilot-control device BDFT and NMA TFs,

$$(32a) \qquad H'_{BDFT}(s) = \frac{b_{BDFT}}{s^2 + (a_1 - b_{NMA} \cdot C)s + a_2},$$

$$(32b) \qquad H'_{NMA}(s) = \frac{b_{NMA}}{s^2 + (a_1 - b_{NMA} \cdot C)s + a_2},$$

acting on the damping ratio of the biomechanical pole. It should be noted that the term b_{NMA} is negative, hence the introduction of the simple linear damper returns a higher damping ratio on the pilot-control device dynamics.

3 LOOP CLOSURE ON THE VERTICAL AXIS

The loop is closed by feeding the pilot-control device BDFT to the tiltrotor AE model through the appropriate gear ratio between the collective pitch rotation and the power-lever vertical displacement, equal to $G_0 = \partial\vartheta_0/\partial\delta_{PL}$ = 1.6 deg/in for the analyzed HEMODE configuration (see Table 8a-IV of Ref. [26]). The PL might also consider an addtional input δ'_{PL} (e.g. due to the voluntary pilot) added to the pilot's BDFT contribution, which yields

$$(33) \qquad \delta_{PL} = H_{BDFT}(s)\ddot{z} + \delta'_{PL},$$

fed into the tiltrotor TF of Eq. 22 through the collective pitch gear ratio,

$$(34) \qquad \left(1 - G_0 H_{BDFT} H_{\ddot{z}\vartheta_0}\right)\ddot{z} = G_0 H_{BDFT} H_{\ddot{z}\vartheta_0}\delta'_{PL}.$$

The Loop Transfer Function (LTF) is thus the coefficient of $\ddot{z}$ in Eq. 34 minus 1, namely:

$$(35) \qquad H_{LTF} = -G_0 H_{BDFT} H_{\ddot{z}\vartheta_0}.$$

With the proposed SISO analytical model it is possible to investigate the stability of the PVS and the sensitivity of the stability to several design parameters. Instead of using the classical eigenvalues investigation, in this case it is possible to exploit the robust stability analysis approach, because it gives information about the grade of stability with respect to parameter variations [29, 30]. The Nyquist criterion is very explicative because it intuitively express the stability degree of robustness as the distance of each point of the LTF frequency response from the point $(-1 + j0)$ in the Argand diagram (see chapter 7 of Ref. [31]). Robust stability indices are phase (P_M) and gain (G_M) margins. The phase margin is the phase difference between the crossing of the LTF with the unit circle and -180 deg., namely $180 - \angle H_{LTF}\left(j\omega_{|H_{LTF}|=1}\right)$. The gain margin is $1/H_{LTF}\left(j\omega_{(-180)}\right)$, i.e. the inverse of the LTF magnitude at ω corresponding to -180 deg. of phase. Positive margins indicate a stable system, while to obtain robust systems is usually necessary to reach gain margins above 6 dB and phase margins of 60 deg.

3.1 Stability predictions

Results in the present section highlight the proneness of the XV-15 tiltrotor to collective bounce according to the simplified AE model. Initially, the Mayo's ectomorphic TF has been introduced in the LTF of Eq. 35. The robust analysis (see Fig. 7) returns an unstable condition characterized by negative gain and phase margins. The PVS shows that the direct effect of a change in collective input results in a nearly immediate change in thrust, which accelerates the tiltrotor exciting the poor damped 1st SWB and, in turn, the pilot's biomechanics. The phenomenon appears as a resonance between the two modes, hence completely different from the collective bounce mechanism triggered in helicopters, in which the highly damped first rotor collective flap mode (rotor coning) reduced the phase margin of the pitch-heave loop TF [9]. In tiltrotors, it is rather the gain margin that is depleted when the pilot-control device BDFT closes the feedback loop with the low-frequency aircraft structural dynamics.

These results must be considered as representative, since several approximations have been introduced in the PVS. In fact, it should be remembered that the proposed AE tiltrotor model is conservative for collective bounce analyses, since it is characterized by an overestimated control derivative T_{ϑ_0} and it neglects the stabilizing effect due to the power-lever friction. The PVS is also characterized by several uncertainties: the pilot-control device BDFT identified by Mayo have been obtained on a flight simulator that differ from the XV-15 cockpit with dissimilar control-device dynamics, besides the strong impact of the neuromuscular activity discussed at the beginning of this work.

Nevertheless, there are two keypoints making the tiltrotor prone to the collective bounce phenomenon:

1. the closeness of the 1st SWB frequency with the pilot's biomechanical pole;

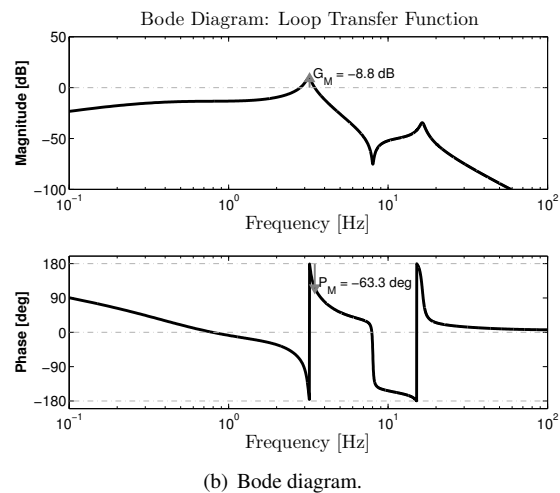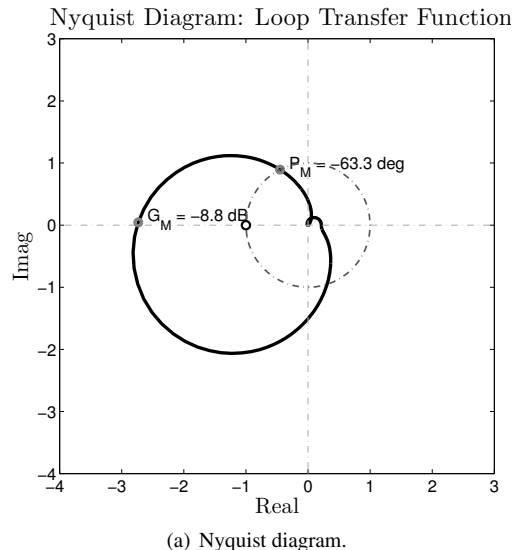(a) Nyquist diagram.

(b) Bode diagram.

Figure 7: LTF with Mayo's ectomorphic pilot-control device BDFT.

2. the poor damping of the 1st SWB mode;

which might bring a PVS close to the resonance. Unfortunately, it is not easy to change the airframe structural frequencies as well as there are not further sources of damping for the 1st SWB mode (in hover condition the wing is not producing any aerodynamic force). From the other side, the pilot-control device BDFT remains the largest uncertainty, since it changes from pilot to pilot and, also considering the same pilot, the biomechanical properties are strictly related to his/her neuromuscular activity.

Sensitivity analyses in Fig. 8 show the bode diagrams of the LTF for several configurations with different gross weight, operationg conditions, pilot-control device models and wing bending stiffness. The PVS are always characterized by negative stability margins. Fig. 8(a) shows the LTF for different values of gross weight. Results are compared between the standard configuration at 13,000 lb and for the light/heavy weight configurations reported in the flight envelope (see Ref. [24]). A change in the gross weight mod-

Table 7: XV-15 analized configurations.

Case no.	Pilot	Gross Weight M_T, lb	Altitude h, ft	Temperature T_0, ^oC	Wing Stiffness EI_{xx}, lb-in^2	Gain Margin G_M, db	Phase Margin P_M, db
1	Ecto	13,000	0.0	15.0	4.40E+9	-8.8	-63.3
2	Ecto	11,000	0.0	15.0	4.40E+9	-10.2	-73.5
3	Ecto	15,000	0.0	15.0	4.40E+9	-7.4	-54.1
4	Ecto	13,000	0.0	-40.0	4.40E+9	-9.9	-67.1
5	Ecto	13,000	9000.0	15.0	4.40E+9	-7.1	-57.4
6	Meso	13,000	0.0	15.0	4.40E+9	-7.0	-45.5
7	Ecto	13,000	0.0	15.0	3.70E+9	-7.9	-50.8
8	Ecto	13,000	0.0	15.0	5.10E+9	-8.7	-71.9

ifies the frequency of the 1st SWB mode and thus the gain and phase margins of the PVS. Results slightly improve when increasing the tiltrotor gross weight up to 15,000 lb. Increasing the weight, the 1st SWB frequency is reduced (from 3.18 to 3.06 Hz, hence a bit more distant from the ectomorphic pilot's biomechanical pole at 3.38 Hz) and the negative gain/phase margins are reduced. Opposite results are obtained when reducing the gross weight, since the new 1st SWB frequency (3.35 Hz when $M_T = 11,000$ lb) results closer to the pilot's biomechanical pole. Fig. 8(b) shows the LTF bode diagrams for different operating conditions. When operating at ISA -40° C the air density increases of about +23%; when operating at 9,000 ft the air density decreases of about -23%. The air density mainly acts on the control derivative $T_{\vartheta_0} \propto \rho \rightarrow \gamma$, increasing the stability margins at higher altitudes through a reduction of the pilot control effectiveness. Sensitivity analyses for the ectomorphic and mesomorphic pilot-control device BDFT models are shown in Fig. 8(c). Results are quite similar. The critical pilot remains the ectomorphic one. Although the mesomorphic pilot's biomechanical pole is characterized by the lowest damping ratio ($\xi_{Ecto} = 32\%$ vs $\xi_{Meso} = 28\%$, see Table 5), the frequency closer to the 1st SWB mode is related to the ectomorphic pilot, which results closer to the resonance condition. Finally, it is shown that the modification of the wing bending stiffness acts on the wing frequencies, although it is necessary a huge mutation of EI_{xx} to shift the 1st SWB mode out of the pilot's biomechanical influence. Fig. 8(d) shows the different bode diagrams for 3 values of EI_{xx} ranging up $\pm$ 16% from the nominal value. None of these three configurations shows a stable situation. The 1st SWB frequency ranges from 2.93 Hz ($EI_{xx} = 3.7E+9$ lb-in^2) to 3.44 Hz ($EI_{xx} = 5.1E+9$ lb-in^2); still too close to the pilot-control device biomechanical pole. All numerical data obtained with the analyzed configurations are reported in Table 7. The worst case scenario results for case number 2, at SLS ISA condition, with Mayo's ectomorphic pilot and light weight configuration, although a combination of the selected parameters may lead to even worst conditions.

3.2 Means of prevention

The previous discussion highlighted how the collective bounce in tiltrotors is due to the resonance between the pilot-control device biomechical pole and the poor damped 1st SWB mode. Prevention requires to either reduce involuntary collective control, or to reduce its effect on the vertical acceleration of the cockpit. Possible means are:

- apply friction to the power-lever, which requires the pilot to overcome a threshold reaction force to actually move the device;

- modify the combined pilot-control device BDFT acting on the control device dynamics; a possible solution consists in adding an hydraulic damper on the powel-lever to further increses the damping of the biomechanical pole;

- redesign the control-device; for example by replacing the power-lever with the thrust control lever used in the V-22;

- in fully or at least partially augmented tiltrotor, filter the unwanted dynamics at the FCS level.

In this work, two means of prevention are fully described to avoid the collective bounce instability: the first is based on the design of a structural notch filter (active device); while the second is obtained by adding an hydraulic damper, with linear characteristics, to the power-lever (passive device). The design takes into account the XV-15 flight envelope for the analized hover configuration, considering a test matrix for all the combinations of #1 gross weight (11,000 lb $<$ $M_T <$ 15,000 lb), #2 operative conditions (from SLS ISA-40°C to FL090) and #3 pilot-control device BDFT models (ectomorphic and mesomorphic). Once identified the worst case scenario, the devices are designed to obtain a stable and robust PVS, hence with a gain margin above 6 db and a phase margin of (at least) 60 degrees.

Notch Filters (NFs) are supposed to suppress the resonance peaks of the undesired structural modes, expressed in terms of LTF (see Ref. [32]). They are characterized by second-order transfer functions in the form:

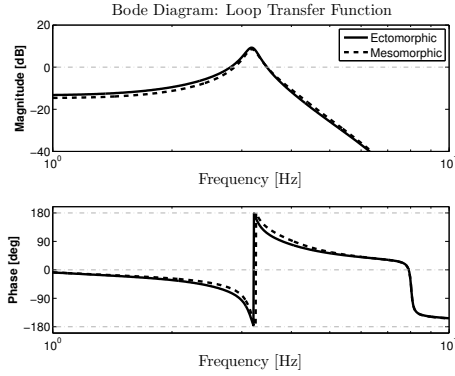$$(36) \qquad H_{NF}(s) = \frac{1 + c_1 s + c_2 s^2}{1 + c_3 s + c_4 s^2},$$

where c_1, c_2, c_3 and c_4 are the NF coefficients. However, it may be useful to adopt a different set of parameters which are more directly related with the NF features. In particular, four parameters can be selected for each NF:
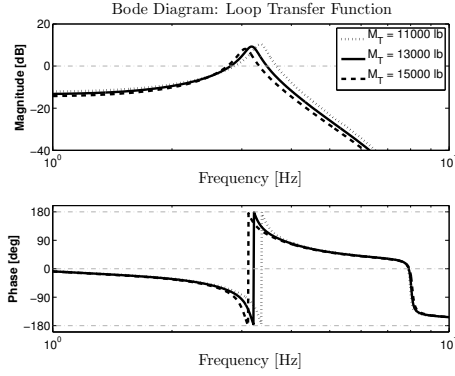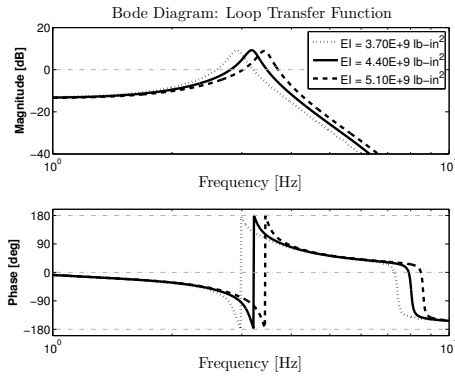
(a) Sensitivity to gross weight.
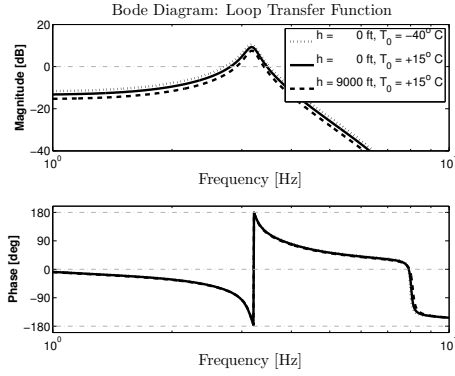
(b) Sensitivity to operating conditions.

(c) Sensitivity to pilot-control device models.

(d) Sensitivity to wing bending stiffness.

Figure 8: Sensitivity analyses to PVS parameters.

1. the notch frequency ω_{NF}, where the maximum decline in gain should be observable;

2. the slope in gain μ (in dB) at the notch frequency;

3. the non dimensional frequency band Breite ξ_{NF}, where the effects of NFs are significant;

4. the non dimensional gain value μ_∞ for infinite frequency.

NF coeffcients and parameters are related to each other through the following expressions:

$$(37a) \qquad \omega_{NF} = \frac{1}{\sqrt{c_2}},$$

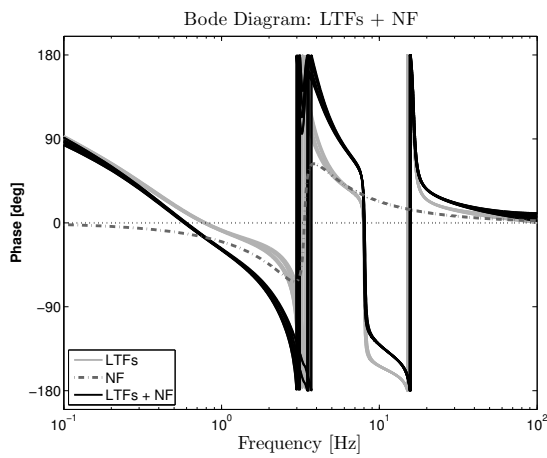$$(37b) \qquad \mu = 20log\left(\frac{c_1}{c_3}\right),$$

$$(37c) \qquad \xi_{NF} = \frac{c_3}{2\sqrt{c_4}},$$

$$(37d) \qquad \mu_\infty = \frac{c_2}{c_4}.$$

In this way, such parameters can be easily selected when analyzing the characteristics of the signal component which should be filtered. The selected parameters have been optimized to make sure that the tiltrotor, equipped with the FCS, satisfies the robust stability criteria. Furthermore, the NF parameters should not be dependent on flight conditions and aircraft configurations in order to achieve a realistic clearance procedure. In this work, a single NF has been designed after an optimization process considering the test matrix defined at the beginning of this section. The LTFs data concerning these different conditions are not managed separately by the optimization algorithm, but an envelope of all flight conditions and configurations is estimated. Results are shown in Fig. 9(a). Starting from the bode diagrams of all the LTFs, the LTF envelope is built. The NF frequency and slope in gain have been selected in order to suppress the highest resonance peak below the threshold of -6 db (ω_{NF} = 3.35 Hz, μ = -25 db) in order to satisfy the gain margin requirement. The non dimensional Breite has been selected in order to maintain the LTF envelope below the threshold of -6 db for all the frequency band close to the NF frequency (ξ_{NF} = 0.6). Finally, a unitary non dimensional gain value for infinite frequency has been chosen to restore the frequency content over the 1st SWB mode. The phase behaviour is shown in Fig. 9(b). The designed NF also satisfies the phase margin requiremet restoring a robust PVS. However, it should be noted that the introduction of NF in the aircraft FCS produces a phase loss in the LTFs (with NF included) that might act in the low-frequency domain, with negative effects on aircraft flight dynamics stability. Hence, in order to accomplish the NF optimization it is necessary to limit its effect only in the frequency range of interest (reducing the Breite parameter). The proposed NF introduces a maximum phase delay of about -20 deg. at 1 Hz and the phase loss is reduced
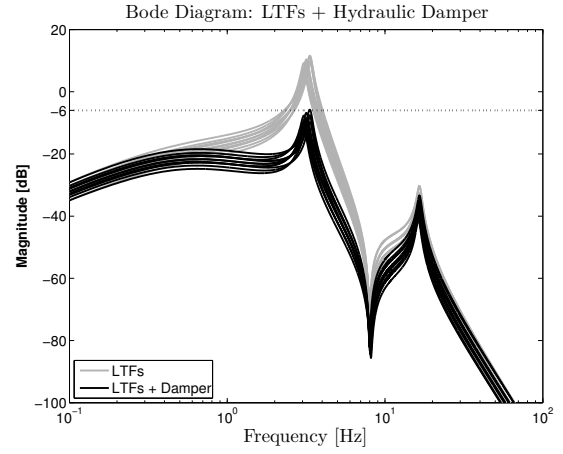
Bode Diagram: LTFs + NF

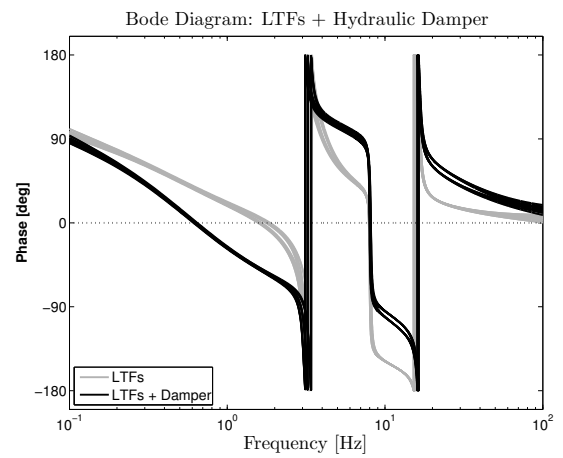(a) Magnitude.

Bode Diagram: LTFs + NF
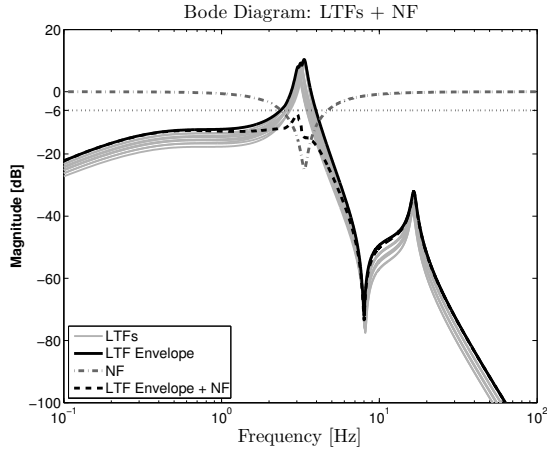
(b) Phase.

Figure 9: Robust design of the NF.

Bode Diagram: LTFs + Hydraulic Damper

(a) Magnitude.

Bode Diagram: LTFs + Hydraulic Damper

(b) Phase.

Figure 10: Robust design of the hydraulic damper.

for the lower frequencies. This solution satisfies the requirements also for the flight dynamics stability, although it should be remembered that the NF has been designed only for the hover condition. When considering the whole tiltrotor flight envelope the optimization procedure for NF design could be more complex, forcing to design scheduled NFs as a function of the flight conditions and aircraft configurations.

The design of the hydraulic damper on the power-lever has been achieved with the modified pilot-control device BDFT of Eq. 32a introduced in the LTF of Eq. 35. In this case, for each condition of the test matrix, the viscous coefficient has been evaluated in order to satisfy the robust stability conditions. Results are shown in Fig. 10. The critical condition has been obtained for the light weight configuration ($M_T = 11,000$ lb), SLS ISA-40°C operating conditions and with the ectomorphic pilot. The designed viscous coefficient is equal to $C = 2500$ Lbf-in/(rad/sec), increasing the damping ratio of the ectomrphic pilot's biomechanical pole from the original $\xi_{Ecto} = 32\%$ to $\xi_{Ecto+C} = 51\%$. This solution is also able to return a stable (and robust) PVS, although it presents several drawbacks: the phase de-

lay effect is not localized in the closeness of the resonance peak but also on the low-frequency flight dynamics bandwidth; moreover the hydraulic damper on the power-lever increases the pilot's reaction force to move the device and to control the vehicle. With the designed hydraulic damper, a pilot's reaction force of about 20 Lbf is necessary to rotate a power-lever with a length of 1 ft at an harmonic input of 1 Hz[§]; clearly an unrealistic force that no pilot would tolerate. The design of an hydraulic damper that stabilizes the PVS, with an acceptable reaction force increment, is still possible although it will not satisfy the robust conditions.

Of course, there exist several means of prevention that have not been included in the previous list; passive absorbers as tuned mass dampers (TMDs) could be mounted directly on the control-device to mechanically notch the undesired pilot frequency as well as on the pilot's seat to suppress the aircraft vibrations that excite the pilot's biodynamics. Similarly, active control laws can be designed in order to increase the damping of the 1st SWB mode. The designer will have to choose the best solution to satisfy the

---

[§]A roughly estimation of the reaction force due to the hydraulic damper is possible in the frequency domain as: $F_C = j\omega C \delta_{PL}$.

robust stability criteria with a thorough evaluation of the side effects that arise from the introduction of a device and that may affect the flight mechanics (and consequently the handling qualities) of the vehicle.

4 CONCLUSIONS

The work describes the collective bounce phenomenon in tiltrotors, a PAO instability that may arise as a resonance between the pilot's biomechanical pole and the aircraft poor damped 1st symmetric wing bending mode. It results different from the mechanism triggered in helicopters, in which the highly damped first rotor collective flap mode (rotor coning) reduced the phase margin of the pitch-heave loop transfer function.

Stability predictions show unstable conditions characterized by negative gain and phase margins. These results must be considered as representative, since several approximations have been introduced in the PVS. The control derivative T_{ϑ_0} has been overestimated and the stabilizing effect due to the power-lever friction has not been taken into account. The largest uncertainty is due to the pilot. The pilot-control device BDFT identified by Mayo and used in this work have been obtained on a flight simulator that differ from the XV-15 cockpit with dissimilar control-device dynamics, besides the strong impact of the neuromuscular activity that may change the pilot's biomechanical response as a function of several factors such as task instruction, spatial position and orientation of the human body.

However, it should be noted that there are two key factors that characterize the tiltrotor as prone to the collective bounce phenomenon: #1 the closeness of the 1st SWB frequency with the pilot's biomechanical pole and #2 the poor damping of the 1st SWB mode (reduced in hover condition since the wing is not producing any aerodynamic force). Sensitivity analyses for different gross weight, operating conditions, pilot-control device BDFT models and wing bending stiffness show that it is not easy to find out the design parameters to avoid the collective bounce, although several means of prevention are available. Two examples are reported: a structural notch filter on the collective control path and an hydraulic damper on the power-lever. Both are able to stabilize the vehicle with robust stability margins, even if some drawbacks are present. The notch filter is usually optimized for one particular flight condition or aircraft configuration. The design of a single (and robust) notch filter for the whole tiltrotor flight envelope does not seem possible. Scheduled NFs, as a function of the flight conditions and aircraft configurations, must be consequently taken into account. The design of an hydraulic damper acts mainly on the damping ratio of the pilot-control device BDFT, restoring a stable PVS. To satisfy the robust stability margins however are necessary large viscous coefficients, increasing drastically the pilot's force to move the device and to control the vehicle.

Future works will be performed on a detailed aeroservoelastic model of the XV-15, in order to provide more accurate results considering the complete tiltrotor flight envelope.

REFERENCES

[1] J.M. Bilger, R.L. Marr, and A. Zahedi. Results of structural dynamic testing of the XV-15 tilt rotor research aircraft. *Journal of the American Helicopter Society*, 27(2):58–65, 1982. doi:10.4050/JAHS.27.58.

[2] T. Parham, Jr., David Popelka, David G. Miller, and Arnold T. Froebel. V-22 pilot-in-the-loop aeroelastic stability analysis. In *American Helicopter Society 47th Annual Forum*, Phoenix, Arizona (USA), May 6–8 1991.

[3] T. Parham, Jr. and Lawrence M. Corso. Aeroelastic and aeroservoelastic stability of the BA 609. In *25th European Rotorcraft Forum*, pages G3–1–10, Rome, Italy, September 14–16 1999.

[4] O. Dieterich, J. Götz, B. DangVu, H. Haverdings, P. Masarati, M. D. Pavel, M. Jump, and M. Gennaretti. Adverse rotorcraft-pilot coupling: Recent research activities in Europe. In *34th European Rotorcraft Forum*, Liverpool, UK, September 16–19 2008.

[5] Marilena D. Pavel, Pierangelo Masarati, Massimo Gennaretti, Michael Jump, Larisa Zaichik, Binh Dang-Vu, Linghai Lu, Deniz Yilmaz, Giuseppe Quaranta, Achim Ionita, and Jacopo Serafini. Practices to identify and preclude adverse aircraft-and-rotorcraft-pilot couplings — a design perspective. *Progress in Aerospace Sciences*, 76:55–89, 2015. doi:10.1016/j.paerosci.2015.05.002.

[6] R. Barry Walden. A retrospective survey of pilot-structural coupling instabilities in naval rotorcraft. In *American Helicopter Society 63rd Annual Forum*, pages 1783–1800, Virginia Beach, VA, May 1–3 2007.

[7] Massimo Gennaretti, Jacopo Serafini, Pierangelo Masarati, and Giuseppe Quaranta. Effects of biodynamic feedthrough in rotorcraft-pilot coupling: Collective bounce case. *J. of Guidance, Control, and Dynamics*, 36(6):1709–1721, 2013. doi:10.2514/1.61355.

[8] Pierangelo Masarati, Giuseppe Quaranta, Linghai Lu, and Michael Jump. A closed loop experiment of collective bounce aeroelastic rotorcraft-pilot coupling. *Journal of Sound and Vibration*, 333(1):307–325, January 2014. doi:10.1016/j.jsv.2013.09.020.

[9] Vincenzo Muscarello, Giuseppe Quaranta, and Pierangelo Masarati. The role of rotor coning in helicopter proneness to collective bounce. *Aerospace Science and Technology*, 36:103–113, July 2014. doi:10.1016/j.ast.2014.04.006.

[10] C. W. Acree, Jr and Mark B. Tischler. Identification of xv-15 aeroelastic modes using frequency-domain methods. TM 101021, NASA, 1989.

[11] C. W. Acree, Jr, R. J. Peyran, and Wayne Johnson. Rotor design for whirl flutter: An examination of options for improving tiltrotor aeroelastic stability margins. In *55st American Helicopter Society*, Montral, Quebec, Canada, May 25–27 1999.

[12] R. Wade Allen, Henry R. Jex, and Raymond E. Magdaleno. Manual control performance and dynamic response during sinusoidal vibration. TR 73-78, AMRL, October 1973.

[13] Henry R. Jex and Raymond E. Magdaleno. Biomechanical models for vibration feedthrough to hands and head for a semisupine pilot. *Aviation, Space, and Environmental Medicine*, 49(1–2):304–316, 1978.

[14] Gordon Höhne. Computer aided development of biomechanical pilot models. *Aerospace Science and Technology*, 4(1):57–69, January 2000. doi:10.1016/S1270-9638(00)00117-6.

[15] John R. Mayo. The involuntary participation of a human pilot in a helicopter collective control loop. In *15th European Rotorcraft Forum*, pages 81.1–12, Amsterdam, The Netherlands, 12–15 September 1989.

[16] Pierangelo Masarati, Giuseppe Quaranta, and Michael Jump. Experimental and numerical helicopter pilot characterization for aeroelastic rotorcraft-pilot couplings analysis. *JAE*, 227(1):124–140, January 2013. doi:10.1177/0954410011427662.

[17] A. Zanoni, P. Masarati, and G. Quaranta. Rotorcraft pilot impedance from biomechanical model based on inverse dynamics. In *International Mechanical Engineering Congress & Exposition (IMECE) 2012*, Houston, Texas, November 9–15 2012. Paper No. IMECE2012-87533.

[18] J. Venrooij, D. A. Abbink, M. Mulder, M. M. van Paassen, and M. Mulder. Biodynamic feedthrough is task dependent. In *2010 IEEE International Conference on Systems Man and Cybernetics (SMC)*, pages 2571–2578, Istanbul, Turkey, October 10–13 2010. doi:10.1109/ICSMC.2010.5641915.

[19] Joost Venrooij, David A. Abbink, Mark Mulder, Marinus M. van Paassen, and Max Mulder. A method to measure the relationship between biodynamic feedthrough and neuromuscular admittance. *IEEE Transactions on Systems, Man, and Cybernetics, Part B: Cybernetics*, 41(4):1158–1169, 2011. doi:10.1109/TSMCB.2011.2112347.

[20] Stefano Zanlucchi, Pierangelo Masarati, and Giuseppe Quaranta. A pilot-control device model for helicopter sensitivity to collective bounce. In *ASME IDETC/CIE 2014*, Buffalo, NY, August 17–20 2014. DETC2014-34479.

[21] Pierangelo Masarati, Giuseppe Quaranta, and Andrea Zanoni. A detailed biomechanical pilot model for multi-axis involuntary rotorcraft-pilot couplings. In *41st European Rotorcraft Forum*, Munich, Germany, September 1–4 2015.

[22] Dale M. Pitt and David A. Peters. Theoretical prediction of dynamic-inflow derivatives. *Vertica*, 5(1):21–34, 1981.

[23] Anderson John D. Jr. *Fundamentals of aerodynamics*. McGraw-Hill, New York, 2010.

[24] M. Maisel. NASA/Army XV-15 tilt-rotor research aircraft familiarization document. TM X-62,407, NASA, January 1975.

[25] Wayne Johnson. *Helicopter Theory*. Princeton University Press, Princeton, New Jersey, 1980.

[26] Samuel W. Ferguson. A mathematical model for real time flight simulation of a generic tilt-rotor aircraft. CR 166536, NASA, 1988.

[27] Samuel W. Ferguson. Development and validation of a simulation for a generic tilt-rotor aircraft. CR 166537, NASA, 1989.

[28] Mark B. Tischler. Frequency-response identification of the xv-15 tilt-rotor aircraft dynamics. TM 89428, NASA, 1987.

[29] Giuseppe Quaranta, Vincenzo Muscarello, and Pierangelo Masarati. Lead-lag damper robustness analysis for helicopter ground resonance. *J. of Guidance, Control, and Dynamics*, 36(4):1150–1161, July 2013. doi:10.2514/1.57188.

[30] Giuseppe Quaranta, Aykut Tamer, Vincenzo Muscarello, Pierangelo Masarati, Massimo Gennaretti, Jacopo Serafini, and Marco Molica Colella. Rotorcraft aeroelastic stability using robust analysis. *CEAS Aeronaut. J.*, 5(1):29–39, March 2014. doi:10.1007/s13272-013-0082-z.

[31] Sigurd Skogestad and Ian Postlethwaite. *Multivariable Feedback Control*. John Wiley & Sons, Chichester, 2005.

[32] M. Battipede, P.A. Gili, L. Carano, and V. Vaccaro. Constrained notch filter optimization for a fly-by-wire flight control system. *l'Aerotecnica Missili e Spazio*, 88(3):105–113, 2009.